# REPORT DOCUMENTATION PAGE

Public reporting burden for this collection of information is estimated to average 1 hour per response, including the time for reviewing instructions, searching existing data sources, gathering and maintaining the data needed, and completing and reviewing this collection of information. Send comments regarding this burden estimate or any other aspect of this collection of information, including suggestions for reducing this burden to Department of Defense, Washington Headquarters Services, Directorate for Information Operations and Reports (0704-0188), 1215 Jefferson Davis Highway, Suite 1204, Arlington, VA 22202-4302. Respondents should be aware that notwithstanding any other provision of law, no person shall be subject to any penalty for failing to comply with a collection of information if it does not display a currently valid OMB control number. **PLEASE DO NOT RETURN YOUR FORM TO THE ABOVE ADDRESS.**

| 1. REPORT DATE *(DD-MM-YYYY)* | 2. REPORT TYPE | 3. DATES COVERED *(From - To)* |
|---|---|---|

| 4. TITLE AND SUBTITLE | 5a. CONTRACT NUMBER |
|---|---|
| | 5b. GRANT NUMBER |
| | 5c. PROGRAM ELEMENT NUMBER |

| 6. AUTHOR(S) | 5d. PROJECT NUMBER |
|---|---|
| | 5e. TASK NUMBER |
| | 5f. WORK UNIT NUMBER |

| 7. PERFORMING ORGANIZATION NAME(S) AND ADDRESS(ES) | 8. PERFORMING ORGANIZATION REPORT NUMBER |
|---|---|

| 9. SPONSORING / MONITORING AGENCY NAME(S) AND ADDRESS(ES) | 10. SPONSOR/MONITOR'S ACRONYM(S) |
|---|---|
| | 11. SPONSOR/MONITOR'S REPORT NUMBER(S) |

**12. DISTRIBUTION / AVAILABILITY STATEMENT**

**13. SUPPLEMENTARY NOTES**

**14. ABSTRACT**

**15. SUBJECT TERMS**

| 16. SECURITY CLASSIFICATION OF: | | | 17. LIMITATION OF ABSTRACT | 18. NUMBER OF PAGES | 19a. NAME OF RESPONSIBLE PERSON |
|---|---|---|---|---|---|
| a. REPORT | b. ABSTRACT | c. THIS PAGE | | | 19b. TELEPHONE NUMBER *(include area code)* |

**FUEL CHEMISTRY AND COMBUSTION DISTRIBUTION EFFECTS ON
ROCKET ENGINE COMBUSTION STABILITY**

The goal of the project is to understand how changes in the rate of energy addition can be used to alter the combustion instability characteristics of liquid rocket engines. Fuels with increased energy, either due to higher heats of formation or energetic additives, will generally result in adiabatic flame temperatures and higher performance. They may have higher rates of reaction. It is known that hydrogen, with a very high rate of reaction, tends to be a stable rocket fuel. This study seeks to understand how changes in combustion rate, due to fuel chemistry changes, might be used to develop high-performing, stable rocket engines .

The overall objective of the project is to develop a fundamental understanding of how the spatial distribution of combustion and its temporal response to pressure oscillations depends on kinetic rates, flammability limits, and energy release density. The comprehensive approach combines basic drop combustion experiments,  an *in situ* study using a spontaneously unstable model rocket combustor, and associated modeling of particles in combustion chamber gas flows.  In the model rocket, mode shapes, growth rates, and heat addition are measured. Fuels with variable energy release rates (eg methane & hydrogen, JP-8 & ethanol), and liquid fuels containing energetic additives (eg hydrides and aluminum) have been studied. The modeling is being used to understand how the particles that may be added to the flow with the energetic additives can be used to provide increased damping.

Specific accomplishments include: definition of the effects on energetic additives on burning drops of liquid fuels; measurement of combustion instability characteristics in a model rocket combustor burning mixtures of methane and hydrogen; detailed study of behavior during stable-unstable transition; and development and validation of a computational model that includes two-phase particulate effects.

## 1      Energetic Additive Characterization and Droplet Burning

### 1.1 Ammonia Borane Additive

The addition of hydrogen can change the combustion of a fuel.   Adding a liquid or solid form of hydrogen is more plausible than adding gaseous hydrogen.    Our objective is to explore the addition of hydrogen via chemically stored hydrogen. Ammonia borane (AB) is a molecule that has the chemical formula $NH_3BH_3$, consists of 19.6 wt.% $H_2$, and can be dissolved into fuels ranging from alcohols to ethers.  AB also contains boron that adds additional fuel to a reaction.  In ethanol, ammonia borane can be dissolved up to 6.5 wt.% allowing up to 1.3 wt.% of the fuel to be $H_2$.  Experiments were conducted using high speed PLIF laser diagnostics and high speed imaging to study the combustion of ethanol with concentrations of AB varying from 0 to 6 wt.%.

When AB is heated in its solid state, it begins to decompose and release $H_2$ gas at several different temperatures depending on the rate of heating.  If AB is kept at a constant elevated temperature for an

extended period of time, decomposition will begin to occur at a temperature of 355 K, near the boiling point of ethanol (351 K).  For higher heating rates the first step of AB decomposition will begin to occur at temperatures below 385 K, releasing primarily $H_2$ with small amounts of borazine.  No significant amount of other products are formed until temperatures exceed 400 K, at which point $H_2$ gas is formed. These results indicate that AB will certainly decompose and release $H_2$ gas while ethanol is burning.

## 1.2 General Observations

The ignition processes for ethanol droplets with and without AB have similar behaviors. After ignition, the combustion behavior of the droplets varies with the concentration of AB.  The combustion behavior of the droplets composed solely of ethanol is fairly uniform throughout the burn.  The droplets are surrounded by a light blue flame and exhibit a relatively smooth regression rate except during ignition and extinction transients. Droplets containing AB have a blue and green flame that becomes greener as the droplet is consumed.  Gas generation and bubble formation within the droplet is common with the addition of AB.  These bubbles coalesce and grow, eventually reaching the surface of the droplet.  Once at the surface, the bubbles usually rupture and expel gas and small liquid droplets from the main droplet.  Liquid that has been expelled from the main droplet is indicated by the arrows in Figure 1.1. This behavior influences the local droplet regression behavior as the droplet can grow or regress; however, the overall regression rate follows the typical $D^2$ law behavior, but has a faster regression value than neat ethanol.  These droplets also typically experience a change in the apparent regression rate when the droplet size becomes comparable to the bead size. As droplet approaches the end of its lifetime, the liquid becomes more viscous allowing for larger bubbles to form within the droplet.  The rupture of these large bubbles can often cause the droplet to shatter and atomize the remaining fuel into small droplets that burn very quickly.  The result of such an event is shown in the ($4^{th}$ frame of Figure 1.1).

PLIF measurements also show a change in the OH reaction zone when 6 wt.% AB is added to ethanol. The OH field becomes more elliptical as its height increases and becomes more off centered from the droplet as the effects of natural convection are augmented.  The eruption of large bubbles within the droplet and subsequent jetting of vaporized fuel can also cause significant deformation of the OH reaction zone as seen in the $4^{th}$ frame of Figure 1.1. There are two major effects that AB has on the combustion behavior of ethanol that we will address further.  These are: 1) the increased regression rate of the droplet, and 2) the notable changes in the combustion behavior of the fuel as it becomes more viscous at the end of the droplet lifetime.
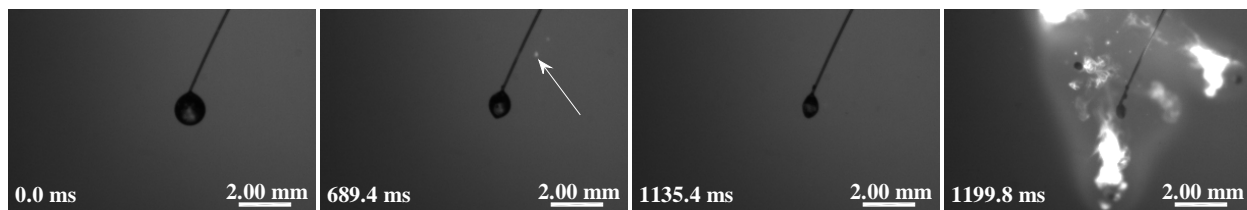
(a)
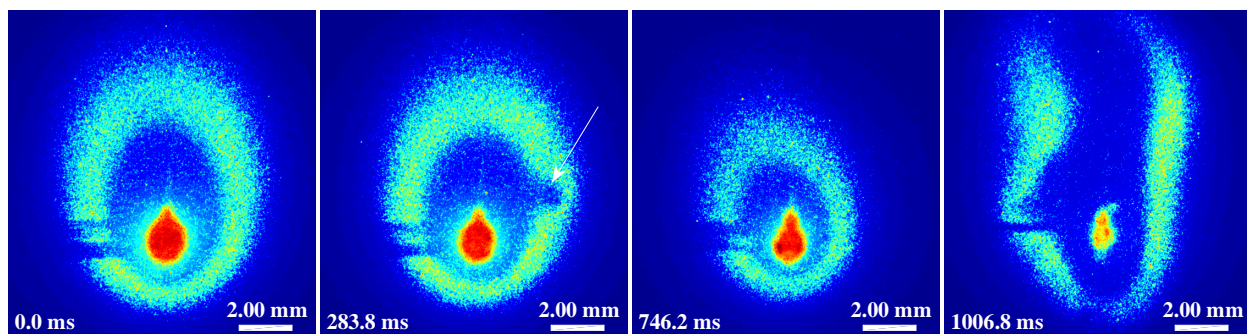


(b)

Figure 1.1: Combustion behavior of ethanol with 6 wt.% AB shown with frames from visual and PLIF measurements.  Arrows indicate liquid that has been ejected from main droplet.  (a) Visual images of droplet burning.  (b) PLIF measurements of separate droplet burning.

### 1.3 Droplet Regression

Ammonia borane has a noticeable effect on the regression rate of ethanol.  Figure 1.2 shows the droplet diameter size history as a function of time during the quasi-steady burning process for both ethanol and ethanol with 6 wt.% AB droplets.  Droplet burn rates are found from the slopes of the lines shown here as well as the droplet regression history for other droplets.  The regression rates are taken from the first part of the regression history before the burn rate decreases.  The measured burn rate for neat ethanol is 0.80 mm$^2$/s with a standard deviation of ±0.05 mm$^2$/s.  Adding 6 wt.% of AB increases the burn rate of ethanol to 0.93 mm$^2$/s with a standard deviation of ±0.08 mm$^2$/s.  This represents a 16% increase in the burn rate of the droplet. AB/ethanol drops burn much more unsteadily. There are several factors that can contribute to this measured increase including the gas generation within the droplet leading to the ejection of small quantities of fuel, the enhanced effects of natural convection, the influence of finite-rate chemistry, and the change in the burn rate itself due to the change of the fuel constituents.
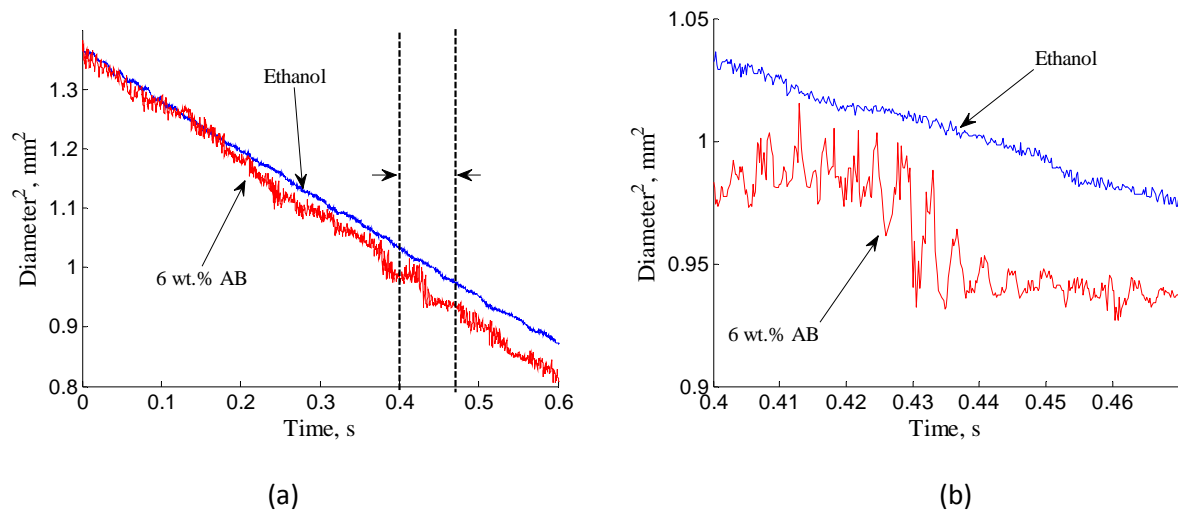
(a)                                          (b)

Figure 1.2: Burning regression rate of neat ethanol and ethanol with 6 wt.% AB.  The overall general behavior is shown in (a) as well as a close up (taken from between the dashed lines) of the local oscillatory behavior of ethanol with 6 wt.% AB (see (b)).

### 1.4  Gas Generation

Gas generation and subsequent bubble formation within the droplet plays several key roles in the dynamic combustion behavior of the fuels containing AB.  As the bubbles grow within the droplet, the droplet begins to swell, thus increasing the surface area of the droplet and the amount of evaporation of the fuel at the droplet surface. And the amount of heat transferred back into the droplet.  These effects continue even after the bubble bursts.  This is because the bursting of the bubble sends ripples throughout the droplet causing the diameter to oscillate as seen in Figure 1.2.

### 1.5  Natural Convection

There are several indications that the addition of AB to ethanol is augmenting the effects of natural convection.  Comparing measurements taken from the PLIF system clearly show the augmentation of natural convection as can be seen in Figure 1.3.  This figure shows the OH band around droplets containing 0, 3, and 6 wt.% AB respectively that corresponds to reaction zone and thus the flame zone of the droplet.  The images are averaged over 4.2 ms and false coloring is added for clarity to distinguish the differences of intensity within the measurement.  Multiple measurements of the different fuels are made, but only three are shown here.  These images have the same general trends observed in the other measurements, even though the measurements are not exactly the same for every droplet from the same fuel and some air currents occasionally affect the flame structure.  The PLIF images show an elongation of the flame structure as well as a shift in the location of the OH band with respect to the location of the droplet as the amount of AB in the fuel increases.  The fuels containing AB clearly move towards the bottom of the OH band as the AB concentration increases resulting from a higher induced flow around the droplet.
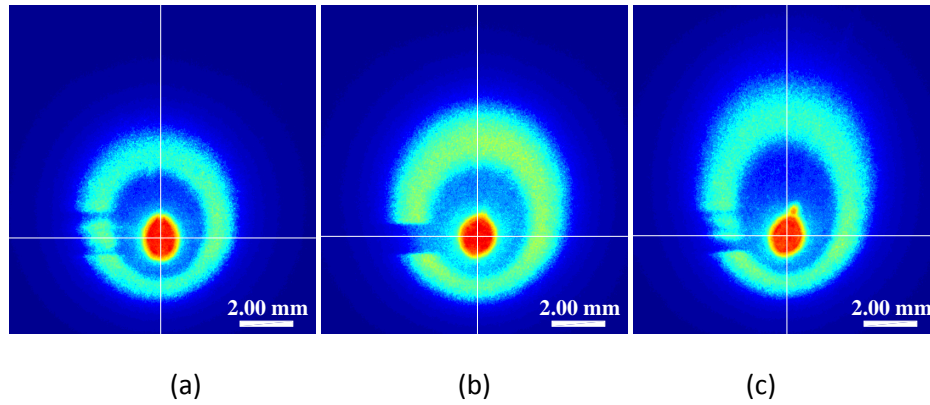
(a)          (b)          (c)

Figure 1.3: False colored PLIF measurements of droplets burning with laser operating at the OH excitation frequency of 283.23 nm and averaged over 4.2 ms. (a) Neat ethanol. (b) Ethanol with 3 wt.% AB. (c) Ethanol with 6 wt.% AB.

These trends continue throughout the quasi-steady portion of the burn as indicated by the data shown in Figure 1.4, which shows the distance between the droplet centroid and the peak of the OH signal as a function of droplet diameter. The data displayed in Figure 1.4 also show an increase in the distance between the peak in the OH reaction and the droplet centroid as the droplet diameter decreases.



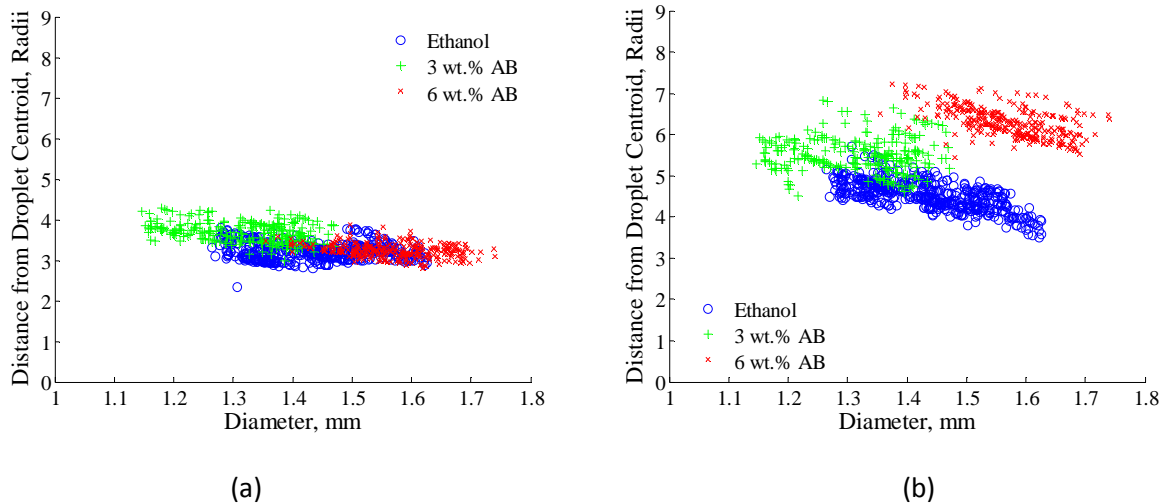(a)                                                  (b)

Figure 1.4: Distance of peak in OH band from droplet centroid as a function of droplet diameter at various locations around the droplet. (a) Right of droplet. (b) Above droplet.

All of these observed changes to the flame reaction zone are consistent with a droplet burning in an environment with increasing natural convection, suggesting that the effects of natural convection are augmented with the addition of AB. The most plausible explanation for this increased convective behavior is the decomposition of AB leading to the release of $H_2$ gas into the fuel vapor. Hydrogen gas is a very light weight, low density gas that rises quickly in the presence of gravity and many other gases

including air.  Its high diffusive rates also allow it to move quickly away from the surface of the droplet. The combination of these two effects will augment the convective flow around the droplet leading to an increase in the transport properties around the droplet and thus an increase in the burning rate.  Its high diffusive rates can also promote better mixing of the fuel and oxidizer.

## 1.5  Decomposition of Ammonia Borane

There are other indicators that AB is decomposing in the droplet or near the surface, supporting the hypothesis that $H_2$ gas is present in the fuel vapors.  One of these indicators is the increase in the amount of OH present in the flame with the addition of AB.  The amount of OH in the flame is sampled in two locations: above and to the right of the droplet.  The relative quantity of OH is found by finding the minimum in the signal intensity between the droplet and the OH reaction zone.  Everything between this minimum and the droplet is assumed not to be OH while everything outside of this minimum is assumed to be OH.  The data obtained from this method is shown in Figure 1.5.  Again, this data shown here is only from three individual droplets taken from the data set, but the data show the similar trends as the overall data set.

The addition of AB to the fuel increases the amount of OH present in the combustion zone around the droplet as can be seen in Figure 1.5.  These observations are consistent with calculations performed in COSILAB that indicate a 5% increase in the OH mass fraction when 1.1 wt.% $H_2$ gas is added to the fuel vapor.  The increase is more noticeable above the droplet than to the right of the droplet.  This is another effect of natural convection that causes the fuel vapor to move upwards above the droplet.



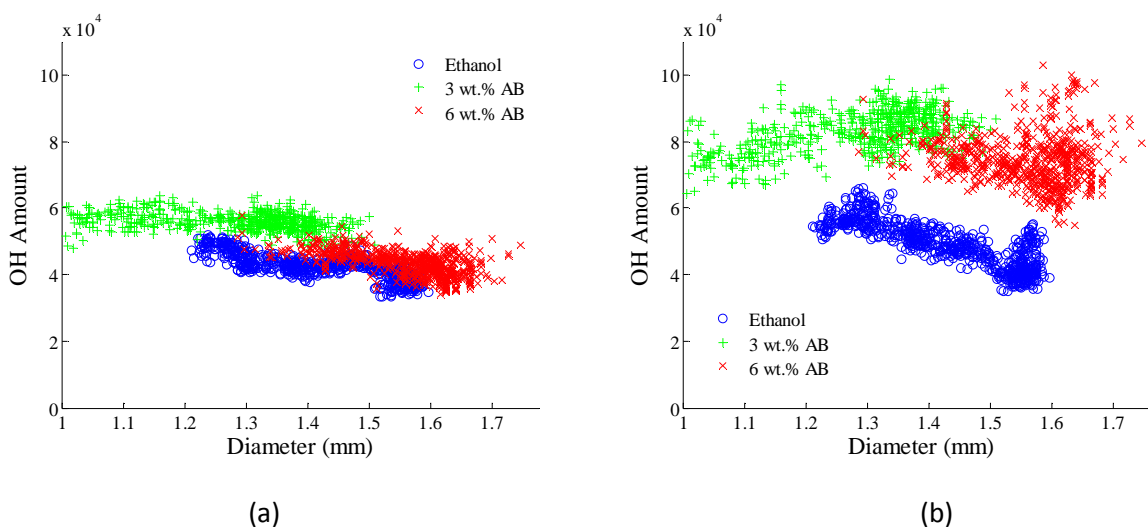(a)                                                          (b)

Figure 1.5: OH signal concentration intensity as a function of droplet diameter in various locations in the flame. (a) Right of droplet.  (b) Above droplet.

## 1.6 Late-Time Viscous Droplet Combustion

Ammonia borane has another significant effect on the combustion behavior of ethanol.  As the liquid fuel is consumed, the ratio of AB decomposition products to liquid fuel increases notably causing the remaining fuel to become more viscous.  The increased viscosity of the fuel impedes the gas generated within the droplet from breaching the droplet surface and thus trapping it.  Along this same time, the gas generation within the droplet notably increases.  The coupling of the increased gas generation with the change in viscosity of the remaining liquid causes the droplet to swell significantly until the droplet shatters causing atomization and rapid combustion of the remaining fuel as seen in the last eight frames of Figure 1.6.  While frames 1-3 represent the quasi-steady burning of the droplet, frames 3-10 show the process that causes a rapid increase in the burn rate and how fast that increase can occur.  The time between the second and third frames and third and tenth frames is the same, but the amount of fuel consumed between the second and third frames is relatively small compared to the amount consumed between the third and tenth frames.  The rapid consumption of the remaining fuel between the third and tenth frames is due to the swelling and shattering of the droplet.  The droplet is burning in all but the first frame even though the spherical diffusive flame cannot be seen in the majority of the frames.
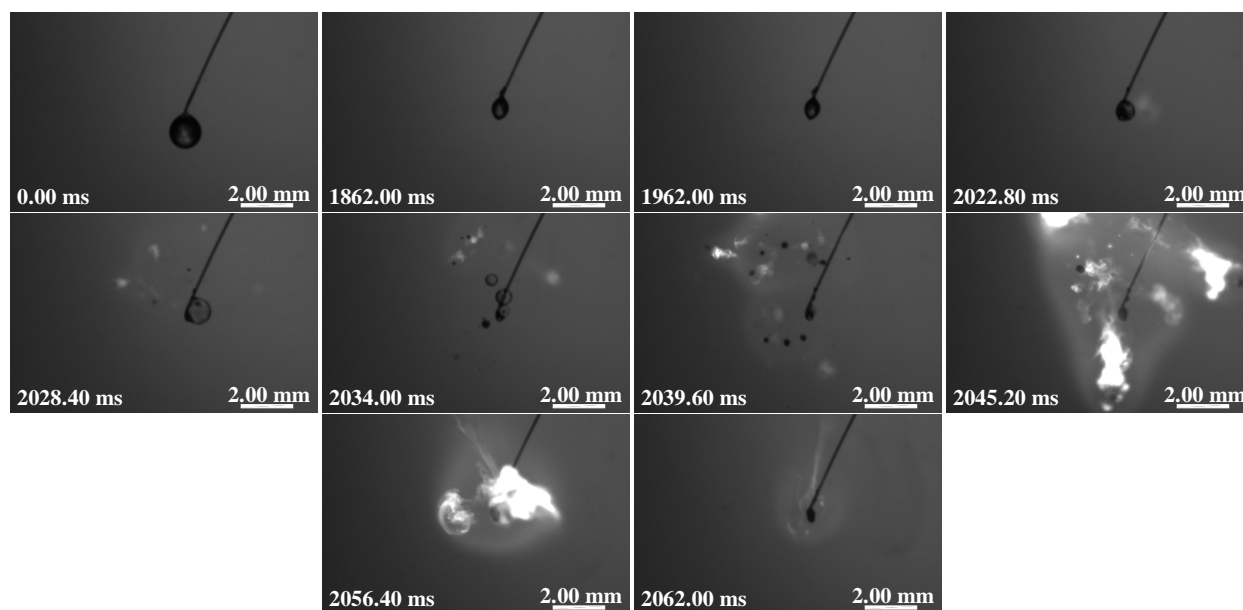


Figure 1.6: Fragmentation of 6 wt.% AB in ethanol droplet with subsequent combustion of fragments in 100 ms at ambient conditions.  The time between the second and third frames and the third and tenth frames is 100 ms.

## 1.7 Nano Aluminum

Droplet burns on a quartz bead were performed on mixtures of nano aluminum (80nm Novacentrix as delivered) and the liquid fuels, ethanol and JP-8.  These burns were observed at 5000 fps.  In order to improve the suspension of nano aluminum in the JP-8, the surfactant, Neodol, was employed.  The qualitative behavior of the combustion of these fluids was observed, and the images are used to determine the burn rate. Nano aluminum concentrations were varied for both liquid fuels in

concentrations of one, two and five weight percent for the ethanol tests.  A neat ethanol droplet, upon ignition, will burn with a very light blue flame and decrease in size until all of the fuel is spent.  An aluminized ethanol droplet will combust much like the neat ethanol initially.  The characteristic bright flashes of burning nano aluminum were not present.  The ethanol burns steadily away, eventually leaving behind an agglomerate of nano aluminum on the quartz rod.  Analyzing the videos showed that these mixtures the concentration of the nano aluminum had an effect on the burning rate.  A 2 wt.% percent concentration of nano aluminum has the highest burn rate coefficient of 0.89 mm$^2$/s, which is faster than neat ethanol's rate coefficient of 0.80 mm$^2$/s.

The JP-8, Neodol, and nano aluminum droplets often resulted in a series of fuel jets and micro explosions at the end of the droplet lifetime.  Upon ignition, a neat droplet of JP-8 will burn orange, and the droplet will regress until all of the fuel is consumed.  An aluminized droplet with Neodol will initially behave the same as a neat droplet.  After some initial burning, the droplet will begin to outgas, ejecting fragments of fuel and nano aluminum, burning with a combination of the orange flames of JP-8 and the bright orange characteristic of nano aluminum.  The pressure inside the droplet eventually builds to the point where a more violent micro explosion will occur, burning the remaining nano aluminum and JP-8.  The intensity of the micro explosions varied based on the amount of nano aluminum added to the mixture.  The remaining nano aluminum would then agglomerate on the quartz rod, though to a lesser extent than for the ethanol nano aluminum mixtures.  The nano aluminum was again varied in concentrations of 1, 2, and 5 wt.% of the whole solution, and Neodol was kept at 3 wt.%.   The intensity of the micro explosion increased with a greater concentration of aluminum, as shown in the pictures below.  There is a large difference between the brightness of the 1 wt. % and the 2 wt. %, while the 5 wt. % is only slightly brighter than the 2 wt. %.
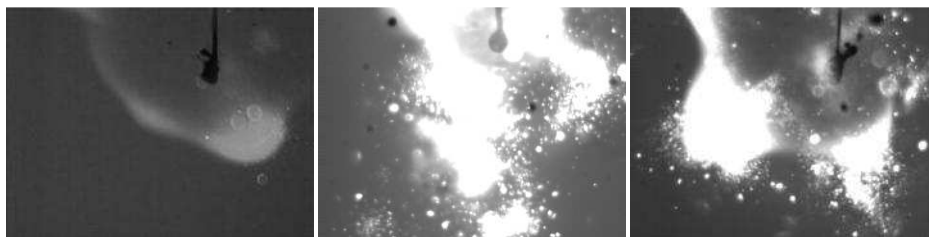


Figure 1.7: Micro explosions of droplets for JP8/Neodol (3 wt.%) with nano aluminum in concentrations of 1 wt.% (left), 2 wt.% (middle) and 5 wt.% (right).

## 2       Hydrogen Addition Effects on Unstable Methane Combustion

Combustion instability was studied using a continuously varying resonance combustor (CVRC) at Purdue University. The capability exists to vary the length of the oxidizer post during a test, thus changing the resonant acoustic frequencies of the combustion chamber. In this way, it has been shown in the past at Purdue that with 100% methane as the fuel, combustion begins stable at an ox-post length (LOP) of 7.5 in, and then spontaneously transitions to unstable combustion as the post decreases in length.

Combustion again spontaneously transitions back to stable combustion once the post has decreased in length to near 4.5 in.

It has been suggested that the addition of hydrogen to the fuel will have an effect on the stability of combustion because of the increased flame speed observed with hydrogen. Chen et al. determined that for a certain percent of hydrogen in methane, the flame speed increases as shown in Figure 2.1
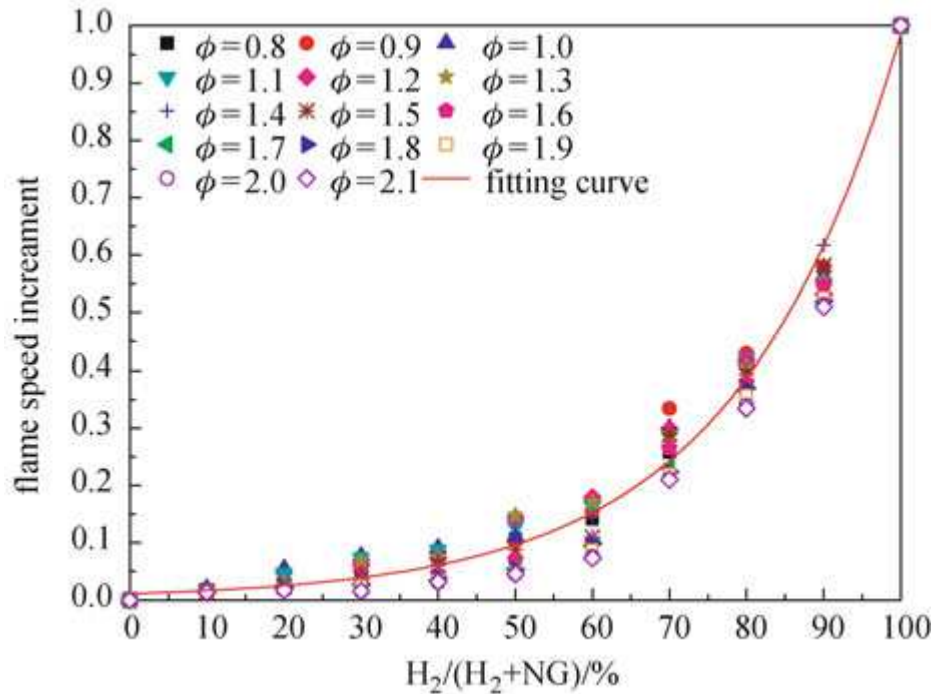


Figure 2.1: Experimental study on the laminar flame speed of hydrogen/natural gas/air mixtures (Chen Dong, Xi'an Jiaotong University, Xi'an 710049, China) © Higher Education Press and Springer-Verlag Berlin Heidelberg 2010

To determine the effect of hydrogen on combustion instability, the CVRC was operated at baseline cases of 0% hydrogen and 100% hydrogen as well as an intermediate case of 80% hydrogen addition by volume. 80% hydrogen was chosen because it is at this mixture that there is a significant increase in flame speed.

## 2.1 Experimental Setup

The present work builds off work previously done at Purdue University by utilizing the Continuously Variable Resonance Combustor (CVRC), a naturally unstable rocket combustor, as a test bed for studying combustion instabilities. The CVRC allows for repeatable instabilities to be created and studied in the laboratory. The experiment has the unique ability of continuously varying the geometry of the oxidizer post during hot fire, thus changing the resonance of the system and creating a varying range of combustion instabilities while maintaining constant inlet conditions. The oxidizer post length will be

varied during the course of each test, translating between lengths of 7.5 *in* and 3.5 *in*. This translation takes place over a sufficient time so that the system can be considered "quasi-steady" at each post length.

The CVRC, shown in Figure 2.2, was previously used to test liquid fuels but has been adapted to be able to test gaseous fuels. The system consists of a gas generator used to decompose the liquid $H_2O_2$ into hot oxygen and steam, an oxidizer injector mounted on a shaft that can translate during the course of the test, a co-axial fuel injector, and a dump combustor. The system is instrumented with thermocouples and two types of pressure sensors that take measurements at 500 Hz and 100 kHz. The chamber has three sections, the first of which is removable and interchangeable with a quartz chamber that is used to view combustion at the head end of the combustor. Care was taken to create a system with conditions that are easy for CFD modelers to duplicate.
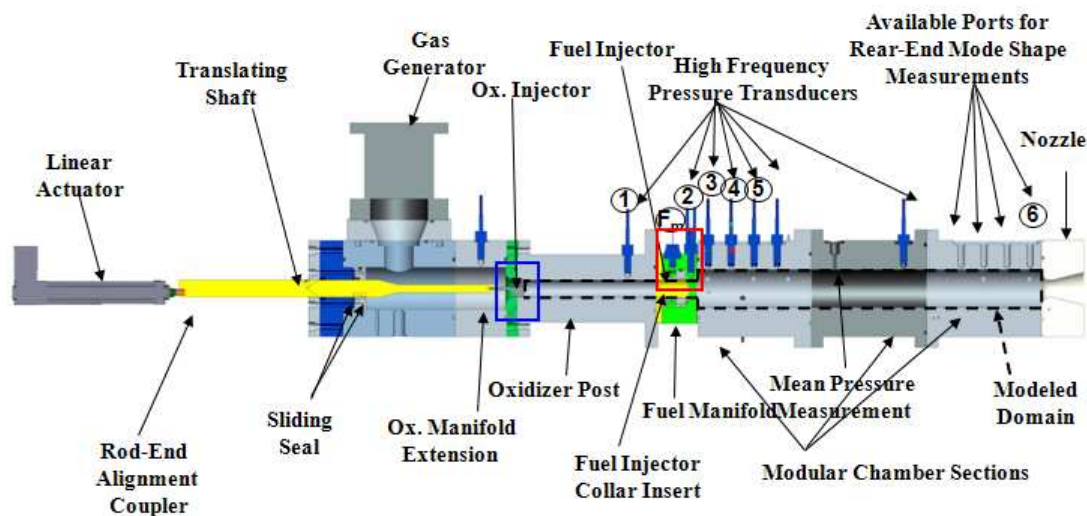


Figure 2.2. Experimental setup of the CVRC combustor. The linear actuator moves the translating shaft providing the variable length oxidizer post. The gas generator is a catalyst bed for the hydrogen peroxide. Pressure is measured along the length of the CVRC by both high and low frequency pressure transducers.

### 2.2 Light Emission from Combustion

High speed videos were taken with a Phantom camera at 10,000 *frames/s* with an exposure of 10 $\mu s$. Each frame contains 184 pixels by 320 pixels, allowing images to be taken across the entire diameter of the combustor and from the injector face to 5.0 in downstream of the injector face. High speed videos of the light intensity were filmed through the optical chamber made of a quartz tube inserted in an acrylic housing.

Chemiluminesence is light emitted by molecules in an excited state when they radiatively relax to a lower energy state. Common high energy chemiluminescent species in hydrocarbon flames include CH*,

OH*, $C_2$*, and $CO_2$*.  CH*, emitting at 432 *nm*, was chosen as the radical to measure for this study because it is present only during the high temperature regions associated with combustion.  Therefore, the light emitted by this radical can serve as a qualitative measure of local heat release.

A Semrock 432/17 narrow band filter with a transmittance of greater than 0.90 for wavelengths in the range of 423-444 *nm* was used on the high speed camera to capture the light emitted during combustion process.  The intensity of the light fluctuates with the combustion and is used as an approximation for the unsteady heat release.  The videos obtained are line of sight measurements.  This induces a degree of uncertainty into the measurements as the light from all sides of the chamber is being recorded.

Local pressure fluctuation values were not recorded during the optical tests because the optical chamber had no instrumentation ports.  The local pressure fluctuations for each pixel location were estimated by applying a time shift and amplitude scaling factor to the pressure measurements made at the aft end of chamber.  Prior experimental data were used to verify that the estimations were accurate.

<p style="text-align:center">2.3 <u>Data Acquisition and Instrumentation</u></p>

Two sets of data were acquired remotely for each test through the use of National Instruments Labview program.  Mean pressure and temperature were recorded at 500 Hz, and high frequency pressure oscillations were recorded at a minimum of 100 kHz.  The 500 Hz data included pressure in both the fuel and oxidizer tanks, before and after the oxidizer catalyst bed, upstream of the cavitating and sonic venturis, in the fuel and oxidizer manifolds, in the oxidizer post, and in the combustion chamber. These measurements were used to obtain the mean pressure data, as they are not capable of collecting data fast enough to capture the high frequency pressure oscillations.   Figure 2.3 shows selected pressures recorded during a typical methane test.  The data show the oxidizer is turned on first and allowed 3.0 *s* to reach a steady operating condition.  The fuel is then turned on and the pressure in the chamber rises.  The odd bump in the oxidizer manifold pressure is caused by the changing volume of the oxidizer manifold as the post translates.  This is consistent and is seen in every test.  The high oscillations in the oxidizer manifold (at 14 *s*) mark the point where the system runs out of oxidizer.  This happens after the test has been completed and the fuel turned off.  The rise in chamber pressure is seen right as the fuel turns corresponds to when the JP-8 enters the chamber.  The system is allowed to reach a steady operating condition before the post begins to translate.

Figure 2.4 shows the calculated mass flow rates of the oxidizer and fuel based on the pressure upstream of the cavitating venturis.  Both flow rates are level indicating the fuel and oxidizer flow was consistent throughout the test.  The fuel flow rate shows a small spike at about 8 s.  This corresponds to when the JP-8 is going through the venturi.  Figure 2.4 also shows the length of the oxidizer post as a function of time.  This is a typical forward translating test.  The post begins at a length of 7.5 *in* and translates at 2.0 *in/s* until it reaches a length of 3.5 *in*.
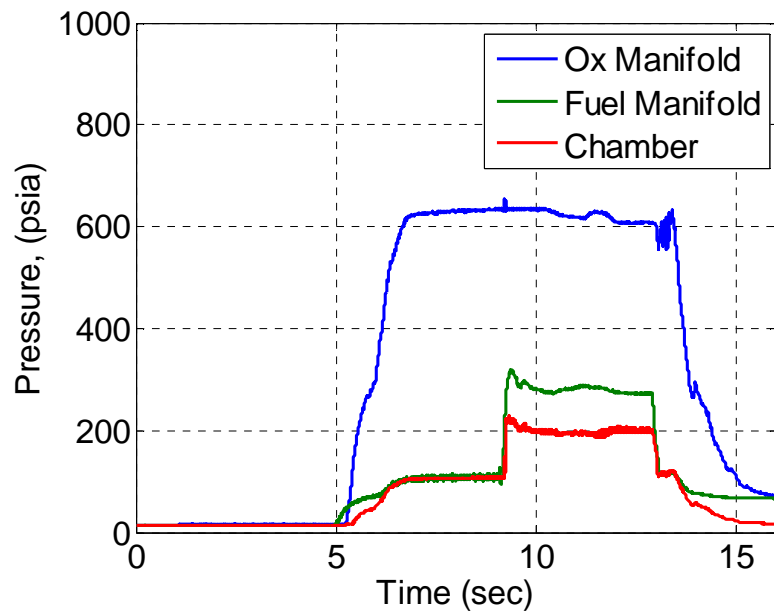
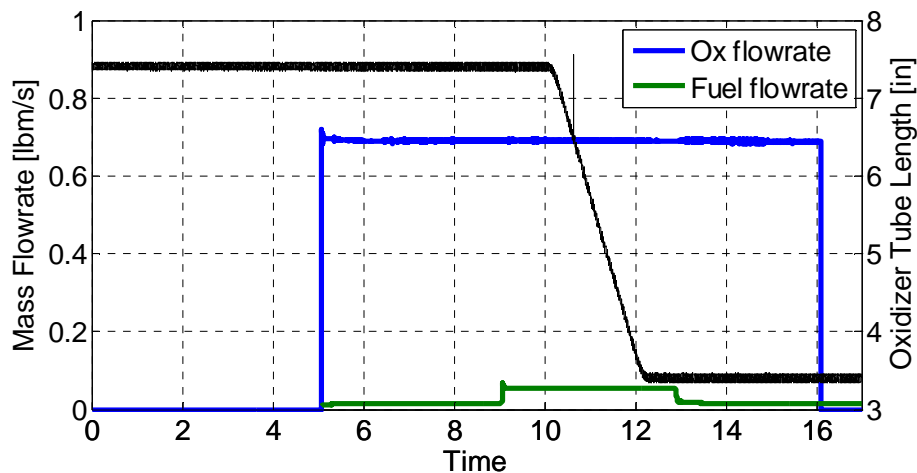Figure 2.3. Pressure data obtained at 500 Hz for a typical methane test.



Figure 2.4. Mass flow rate of the fuel and oxidizer and length of the oxidizer post vs. time for a typical methane test.

To analyze the high frequency pressure measurements obtained during each test, waveform shape, PSD plots, and spectrogram plots were determined. Because it is not possible to measure pressure inside the optical section, all pressure measurement analysis will be done using data obtained from the 14.5" location (near the nozzle) which is present during optical and non-optical tests. This way, pressure data can be directly compared between optical and non-optical tests.

2.4 <u>Pressure Results</u>

The pressure signal can be high-pass filtered at 150 Hz to get rid of any electrical noise in the signal. The resulting high-passed signal can then be examined. The high-passed signal can then be analyzed in the

frequency domain by obtaining the Power Spectral Density of the signal (PSD). The data used to perform the PSD is taken from 0.1s of data. 0.1 seconds corresponds to a post movement of .2 inches. Because of the small length change during this period of time, a quasi-steady assumption is taken for the 0.1 second sample of data. A typical PSD is shown below in Figure2.5.
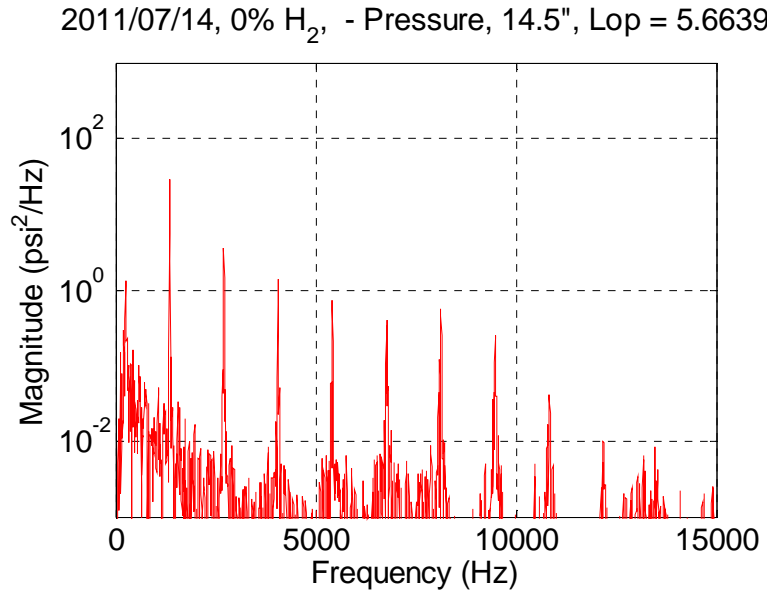
2011/07/14, 0% $H_2$, - Pressure, 14.5", Lop = 5.6639



Figure 2.5. Power Spectral Density plot of the pressure signal from the 14.5" location

It is of interest to see how this PSD taken for 0.1s of data changes throughout the test as the oxidizer post length changes. To do this, a PSD is calculated at each 0.1 second interval and the peak amplitude value corresponding to the first mode is taken at each interval. This value is recorded and then plotted against the oxidizer post length (Lop).  An example of this PSD vs. Lop plot is shown below in Figure2.6.
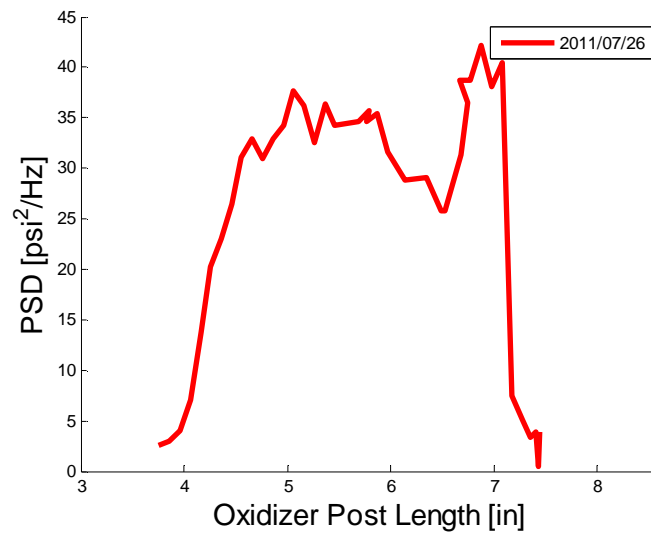
Figure 2.6. PSD vs. Lop for the 14.5" location.

In this particular test, combustion instability as measured from each PSD peak starts off stable at Lop=7.5" As the post transitions, the instability level increases dramatically near Lop=7.0". Different levels of instability are observed throughout the test and the levels decrease back to a stable condition starting near Lop=4.5". In addition to recording each PSD peak amplitude, the corresponding frequency at which the peak occurs can also be recorded and plotted against the oxidizer post length. An example of this PSD(freq) vs. Lop plot is shown below in Figure 2.7.
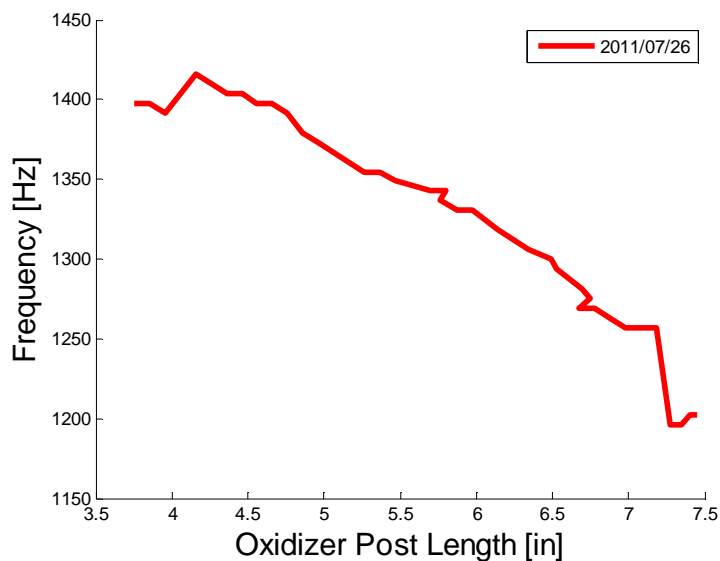


Figure 2.7. PSD(freq) vs. Lop. Showing how the frequency of the first mode changes with a changing oxidizer post length.

Once again, note that the test begins at an oxidizer post length of 7.5". Here we see the 1$^{st}$ mode frequency start near 1200 Hz and transition to higher values throughout the test as the oxidizer post length decreases. It is also worth noting the large jump in frequency near Lop=7.0" which corresponds to the same oxidizer post length at which the test transitioned to unstable combustion. This jump is typical and is seen in the other tests.

## 2.5 High Speed Optical Measurements

In addition to obtaining pressure measurements, each test was performed with the instrumented chamber section replaced with an optically accessible quartz chamber section.  To analyze and compare this optical data for different hydrogen concentrations, the following analysis was performed: Averaged Light Intensity, Total RMS Intensity, 1$^{st}$ Mode RMS Intensity. Because of the large amount of data contained in the high speed image files, the high speed video was broken up into sets of 230 frames. These sets were taken at various times corresponding to various oxidizer post lengths. The 230 frame set contains approximately 30 pressure cycles. The quasi-steady assumption is again made because the post moves only 0.046" during each frame set. In all optical results shown, flow will be from left to right (the injector is on the left).

To obtain the average light intensity, the average of each pixel is taken over the entire frame set. The average light is an indication of where combustion is taking place in the chamber. Because of the problems with the line of sight measurements, the average light intensity is most useful in determining the distance from the injector face that combustion occurs in the chamber.

To determine where the largest fluctuations are occurring in the combustion, the root-mean-squared (RMS) value at each pixel in the frame set is determined from the raw pixel intensity signal. Like the total RMS intensity plots, the 1$^{st}$ Mode RMS intensity plots are created by determining  the RMS value for each pixel. This time, instead of determining the RMS value from the raw intensity signal, the light intensity signal is first band-passed around the first mode frequency. The RMS value is then taken from the resulting band-passed signal. The 1$^{st}$ Mode RMS intensity plot shows where the light is fluctuating the most at the same frequency as the pressure.

## 2.6 Test Conditions

Tests were performed for hydrogen concentrations by volume of 0%, 80%, and 100%. The operating conditions for each test are presented below in Table 2.1 The nominal operating conditions are a chamber pressure of 200 psi and an overall equivalence ratio of 0.8.

Table 2.1.  Summary of experimental test conditions.

| Test Number | 1.1 | 1.2 | 2.1 | 2.2 | 3.1 | 3.2 |
|---|---|---|---|---|---|---|
| Hydrogen Percent (Vol.) | 0% | 0% | 80% | 80% | 100% | 100% |
| Optical? | No | Yes | No | Yes | No | No |
| Chamber Pressure (psi) | 200.00 | 200.00 | 204.00 | 215.00 | 212.00 | 210.00 |
| $H_2O_2$ flow rate (lbm/s) | 0.6900 | 0.7000 | 0.70 | 0.71 | 0.701 | 0.696 |
| $CH_4$ Flow Rate (lbm/s) | 0.0550 | 0.0560 | 0.0285 | 0.0308 | 0 | 0 |
| Oxidizer to Fuel Ratio | 12.5 | 12.5 | 16.7 | 15.8 | 21.5 | 20.2 |
| Equivalence Ratio (Φ) | 0.751 | 0.754 | 0.748 | 0.790 | 0.872 | 0.927 |
| Test Date | 7/14/2011 | 7/26/2011 | 10/24/2011 | 10/26/2011 | 4/6/2010 | 7/6/2011 |

Because there is no CH* emission when burning pure hydrogen with hydrogen peroxide, no optical data was taken for the 100% hydrogen case.  The results for each analysis outlined in the previous chapter will now be compared for each of the three cases of hydrogen concentration.

## 2.7  High Frequency Pressure Measurements

First the high frequency pressure measurements form each hydrogen concentration will be compared. Because it would be difficult to make comparisons directly from the PSD plot alone, the PSD vs. Lop plots are shown below for PSD peaks and corresponding frequencies in Figures 2.8 and 2.9, respectively.
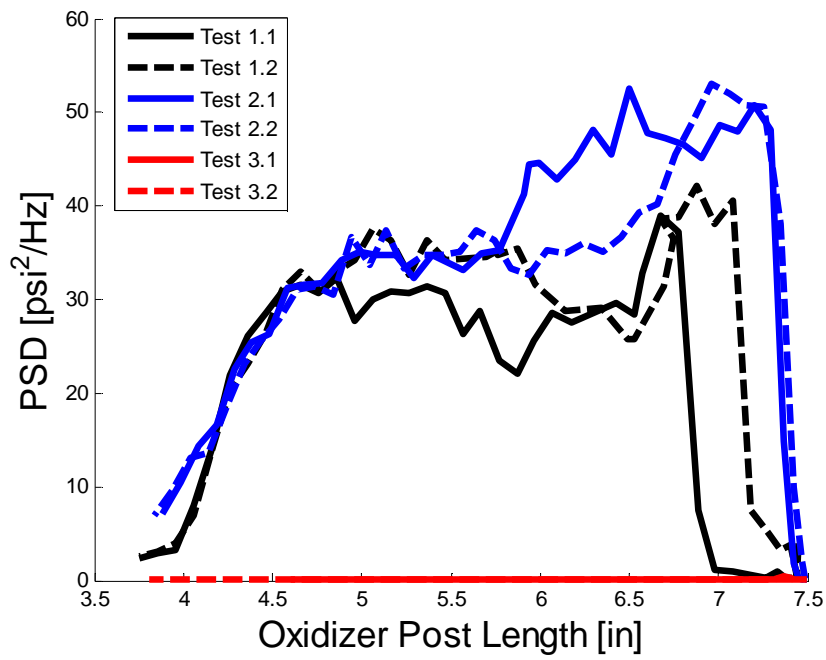
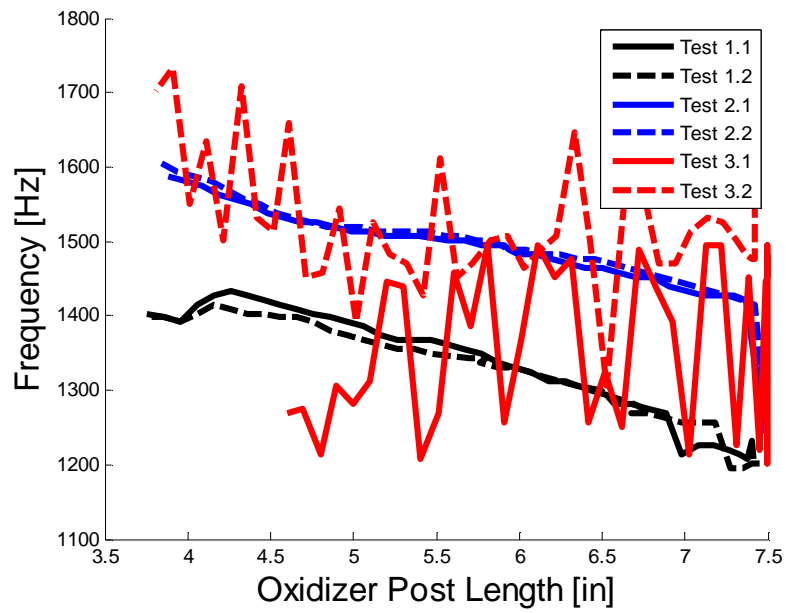Figure 2.8. PSD vs. Lop comparing all six tests.



Figure2.9. PSD(freq) vs. Lop comparing the frequency as a function of oxidizer post length for all six tests.

Again, the legend shows the test number and for simplicity in visualization, black lines are for 0% hydrogen, blue lines are for 80% hydrogen, and red lines are for the 100% hydrogen cases. In the amplitude plot, it is clear that the hydrogen case is not unstable. Because there are no peaks in the PSD plot for 100% hydrogen, it is not possible to pick out a frequency and that is why the frequency appears to jump all over in the PSD frequency plot. The PSD does not yield any insightful data for the 100% hydrogen case except that it is stable.

The PSD vs. Lop does however provide useful information about the 0% and 80% hydrogen addition cases. The 80% hydrogen cases both appear to transition to unstable combustion much sooner than the 0% cases. The 80% hydrogen cases reach a similar, yet slightly higher amplitude than that of pure methane suggesting that the addition of hydrogen at 80% by volume actually increases unstable behavior. The trend throughout the test is very similar for both cases. The high instability levels slowly decrease as the oxidizer post decreases in length and then dramatically start to transition back to stable combustion around and oxidizer post length of 4.5".

The PSD(freq) vs. Lop plot shows that the two cases for 0% and 80% hydrogen have similar trends as the oxidizer post decreases. Both cases show an increase in frequency at a similar rate. Both cases also show a dramatic increase in frequency at the point where the test transitions from stable to unstable combustion. The 80% hydrogen case has a frequency that is roughly 160 Hz higher than the 0% hydrogen case.

A Spectrogram from each test is shown below in Figure 2.10. The test numbers are indicated above each sub-figure. Once again, it is clear right away that the 100% hydrogen case was stable throughout the duration of the post movement. There is however one discrepancy in the 100% hydrogen case. During test 3.2, the hydrogen case actually appears to be operating unstable prior to the movement of the post. This behavior was not captured by the PSD because it did not examine what happened prior to post movement. As soon as the post begins to move, Test 3.2 immediately becomes stable and this behavior continues until the end of the test.

The 0% and 80% hydrogen cases show very similar behavior. During each test, there are initial disturbances due to the ignition of the propellants which die out. Next, the amplitude of instability increases almost instantaneously at a certain oxidizer post length (this length various depending on the test). At this time, even higher order modes, up to 9 of them, appear. As the post continues to translate, the instabilities begin to disappear one by one starting with the higher order modes and working down to the first mode.  Throughout the transitioning portion of the test, it can once again be noticed that the frequency of the instabilities slowly increases with decreasing oxidizer post length.

Note that the spikes observed in the oxidizer post length represented by the blue line are due to electrical noise and are not real. The post transitions smoothly from 7.5" down to 3.5" at a rate of 2" per second.
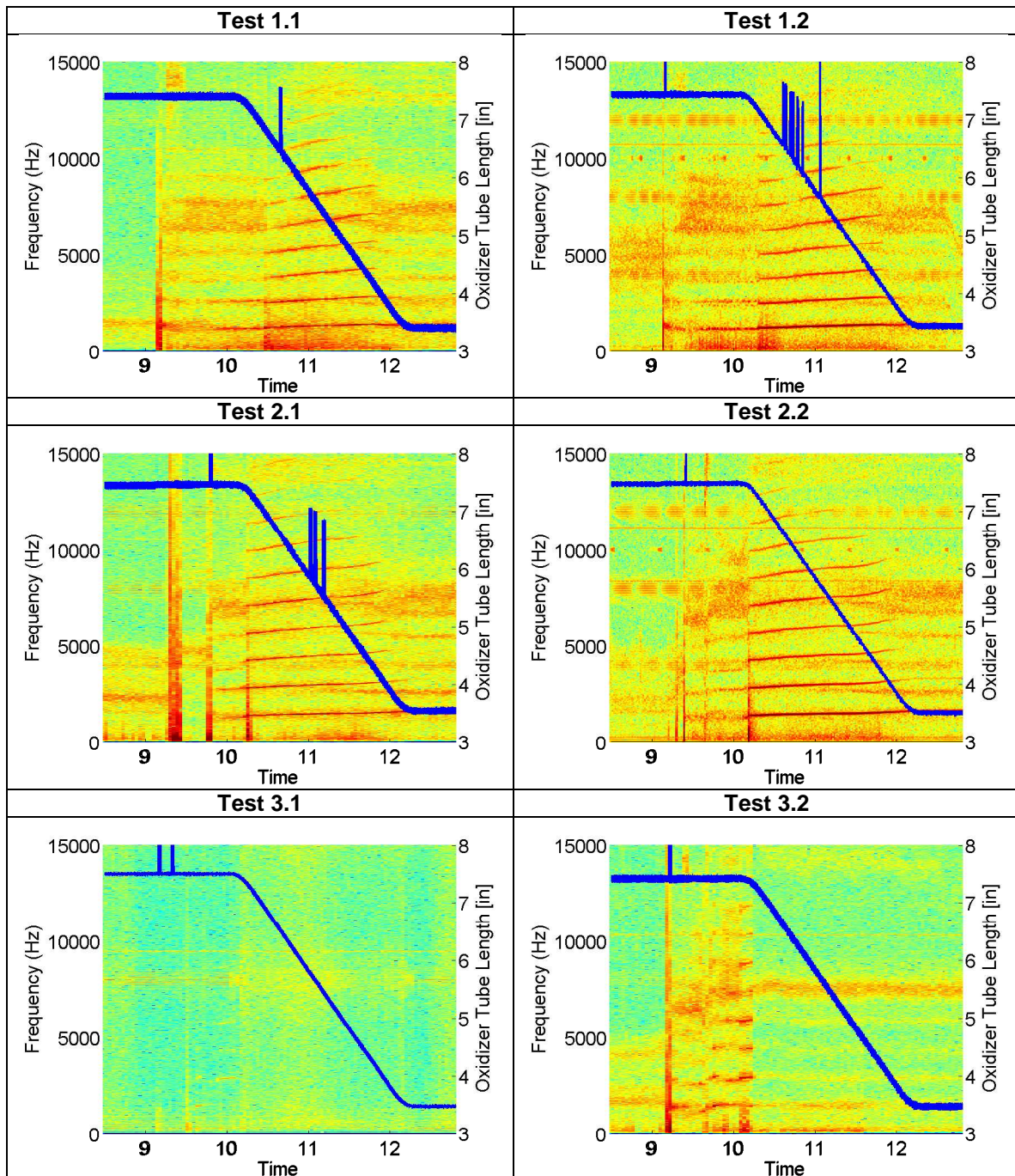
Figure 2.10. Spectrograms from all six tests.

## 2.8 High Speed Optical Measurements

Now that the pressure data for each case has been compared, an investigation into the effects of hydrogen addition using the optical results can be performed. Once again, note that because there is no CH* emission when pure hydrogen is burned with hydrogen peroxide, only optical results for Tests 1.2,

and 2.2 will be shown. (Test 1.1 and Test 2.1 did not have the optical chamber installed). Average light intensity plots for Test 1.2 and Test 2.2 are shown below in Figures 2.11 and 2.12 respectively.  Apart from the difference in intensity magnitude, the two tests appear to behave similarly. Initially, combustion is taking place away from the injector face. As the test transitions from stable to unstable, the main combustion zone moves back closer to the injector face. Likewise, as the test begins to transition to stable combustion, the region of combustion moves back away from the face.
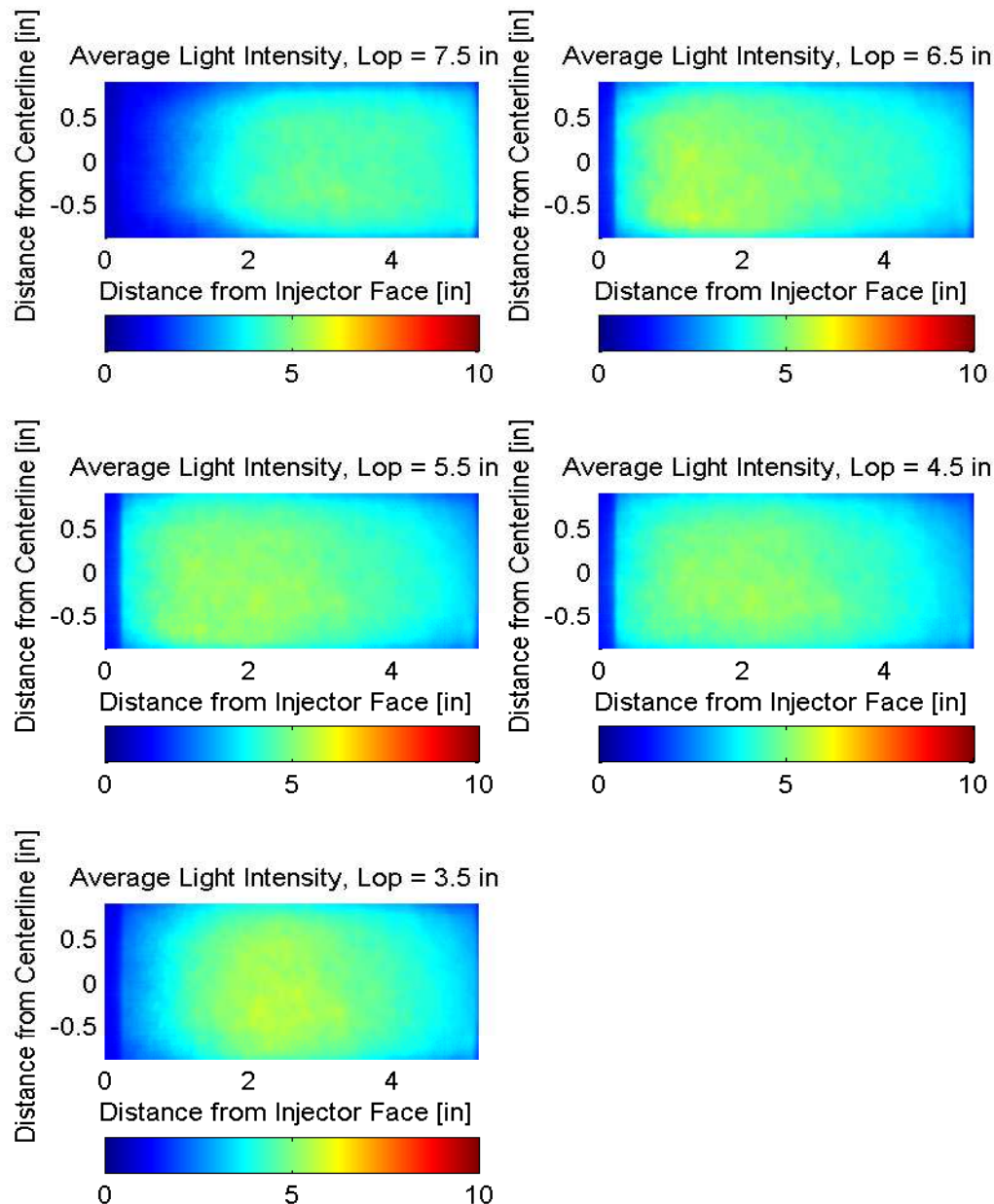


Figure 2.11. Test 1.2 Average light intensity plots for various oxidizer post lengths. 0% hydrogen.
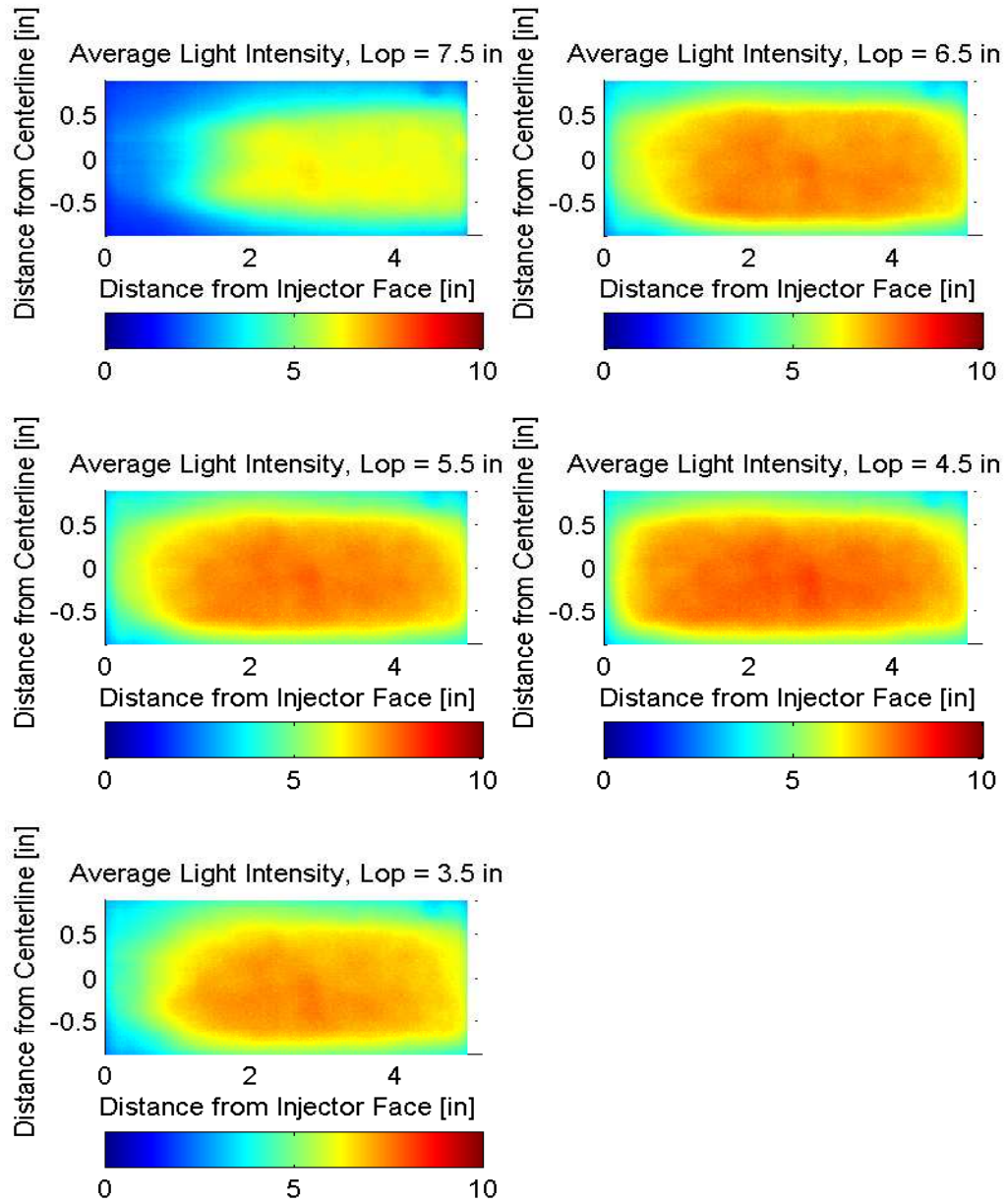
Figure 2.12. Test 1.2 Average light intensity plots for various oxidizer post lengths. 80% hydrogen.

The total RMS intensity is plotted below of Test 1.2 and Test 2.2 in Figures 2.13 and 2.14 respectively. Once again, the first thing that is noticed is that the intensity of the RMS values for the 80% hydrogen case are larger than they are for the 0% hydrogen case. In both cases, the level of oscillations in light are low at the beginning and end of the test. Higher RMS values are seen during the portion of the test which is unstable.
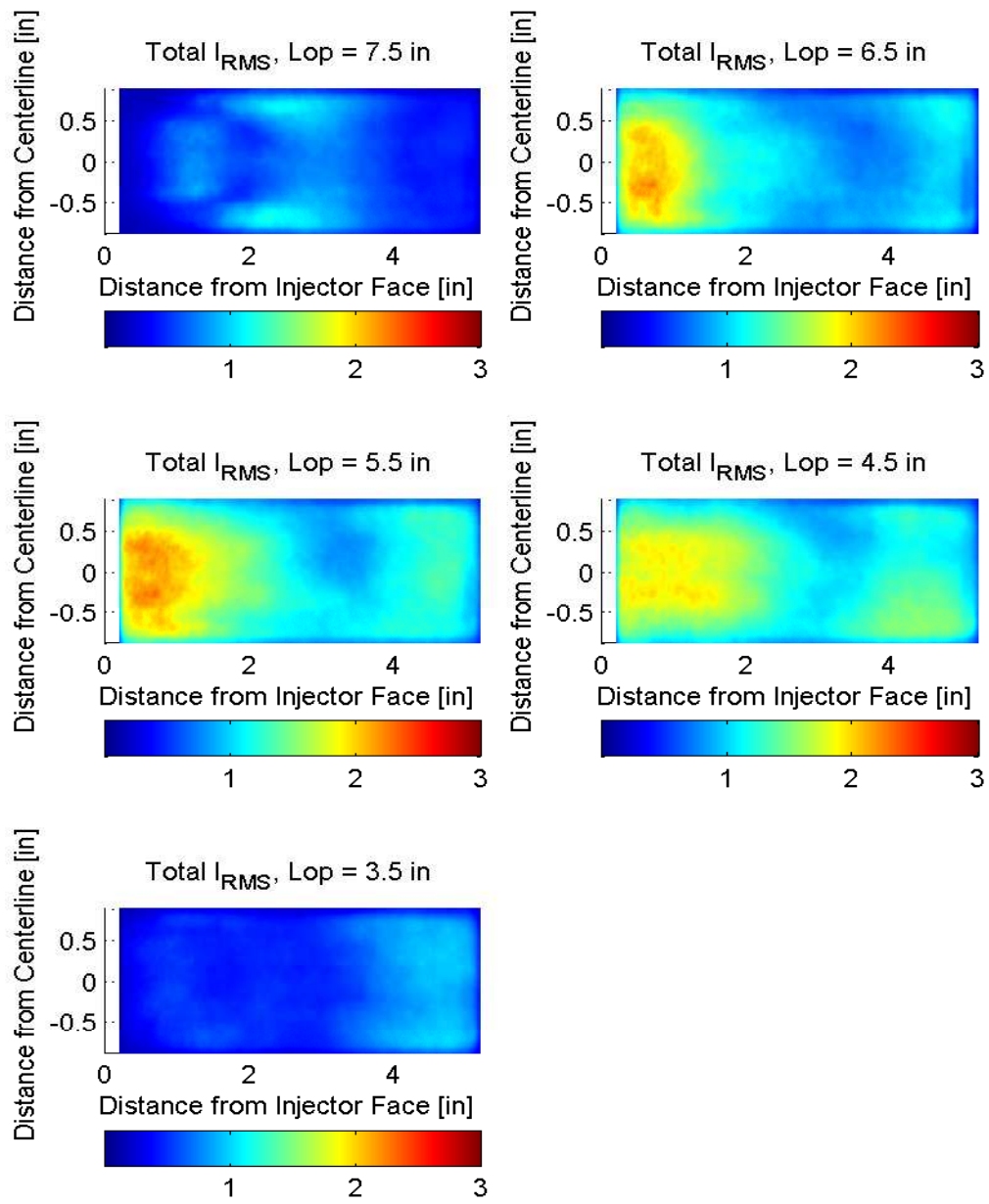
Figure 2.13. Test 1.2 Total RMS light intensity plots for various oxidizer post lengths. 0% hydrogen.
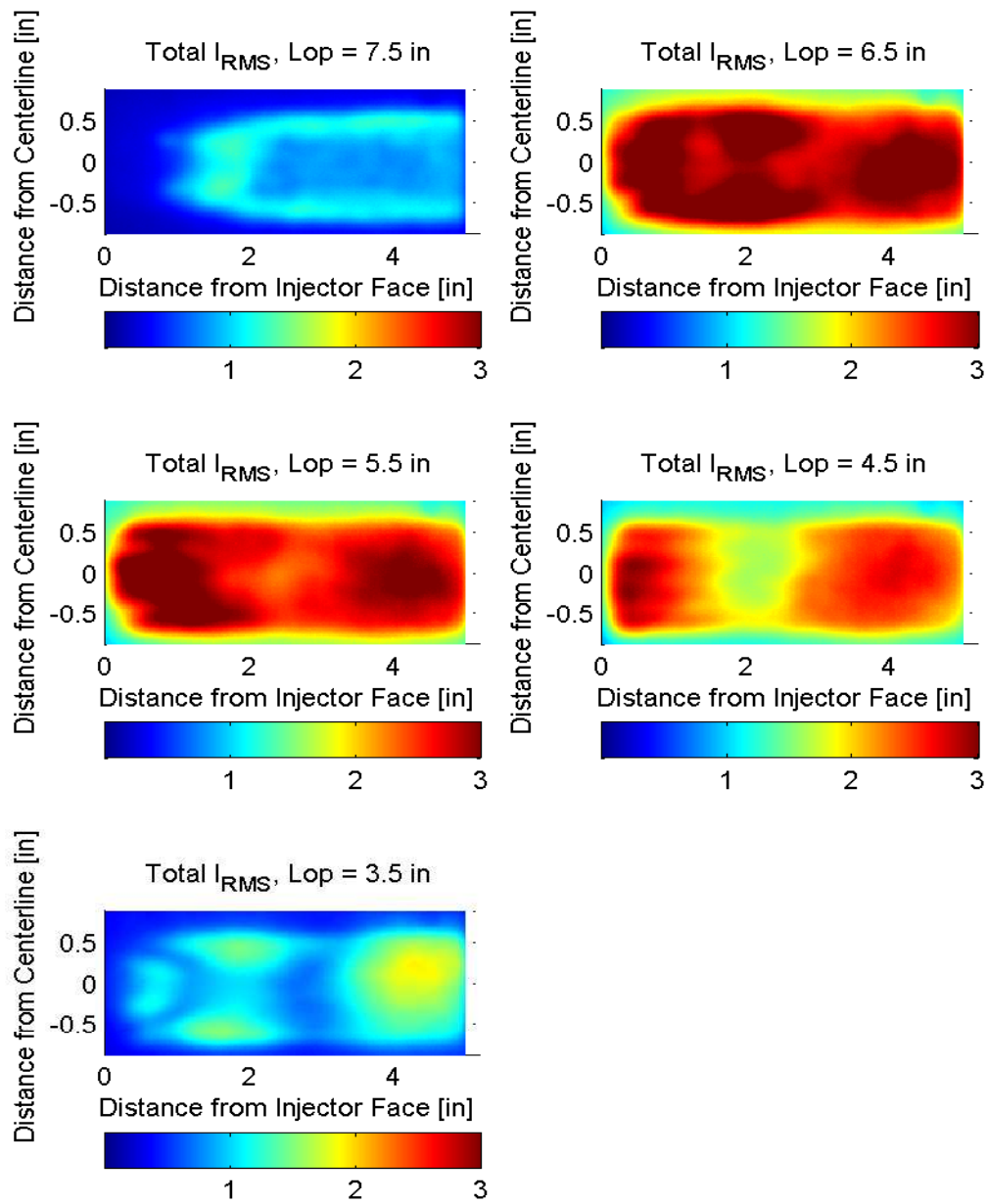
Figure 2.14. Test 2.2 Total RMS light intensity plots for various oxidizer post lengths. 80% hydrogen

The total RMS plots show the first signs of distinction between the two cases. During the 0% hydrogen test, light oscillations appear only near the head end of the injector. Conversely, during the 80% hydrogen test, the oscillations as indicated by RMS intensity are spread across the entire width of the optical section. At an oxidizer post length of 4.5" (corresponding to near the location where the

combustion began a transition to stable combustion), the RMS intensity appears near the injector face and at the downstream end of the optical section, leaving an area in the middle that has low levels of RMS intensity.
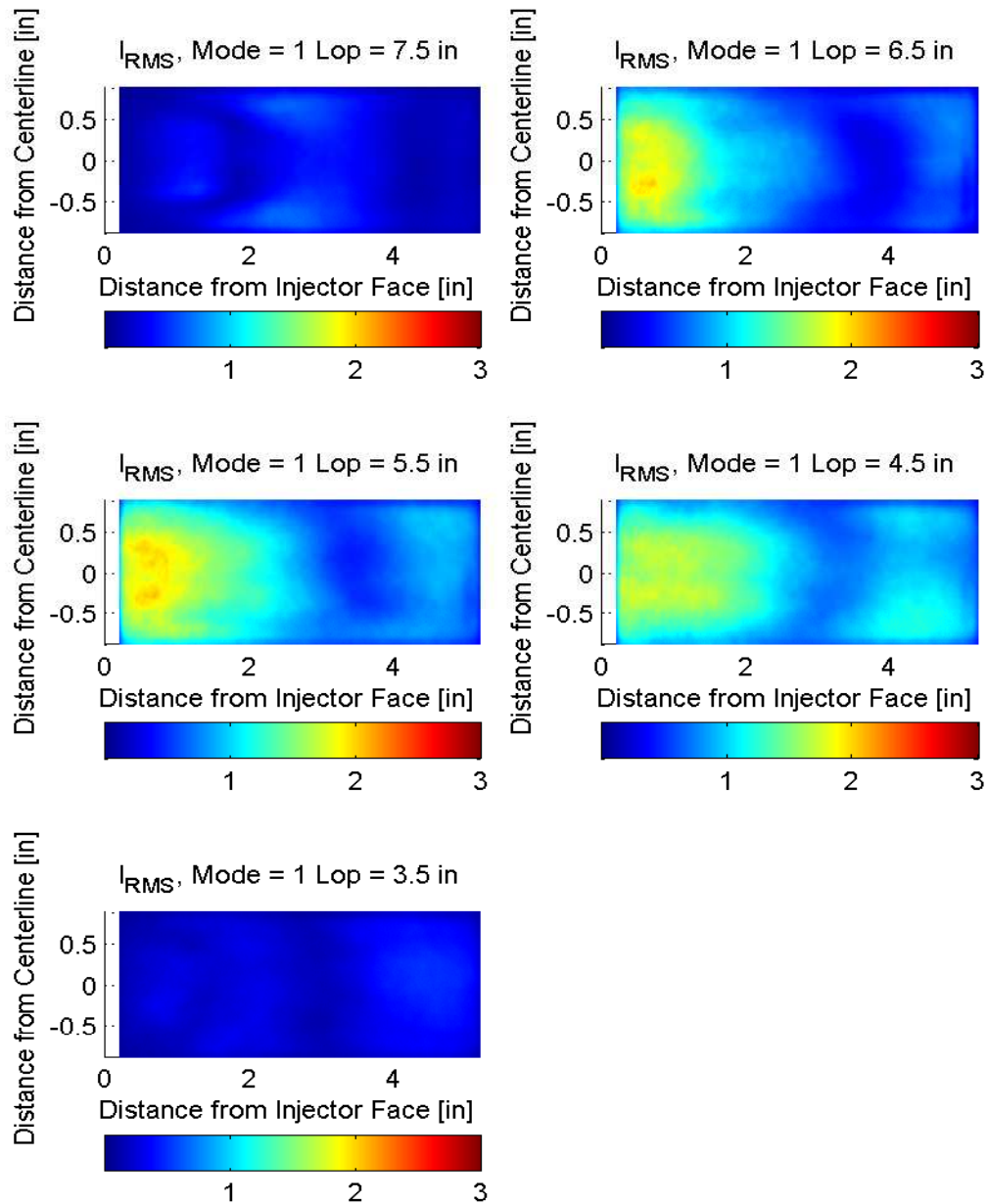


Figure 2.15. Test 1.2 1st mode band-pass filtered RMS light intensity plots for various oxidizer post lengths. 0% hydrogen
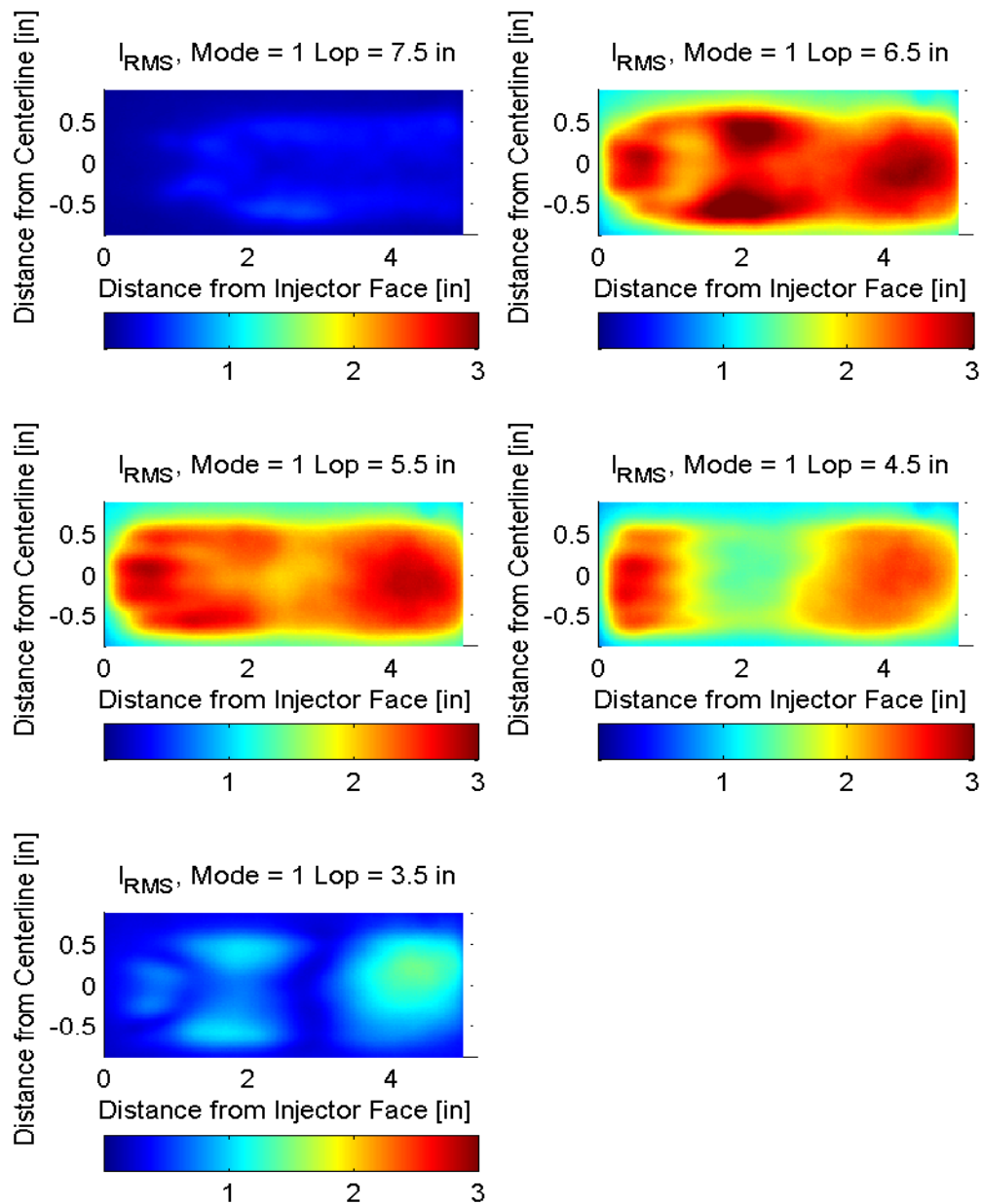
Figure 2.16. Test 2.2 1st mode band-pass filtered RMS light intensity plots for various oxidizer post lengths. 80% hydrogen

## 3    Particle Interactions

### 3.1 Introduction

Metal additives are used to enhance the energy of solid propellants and are also given consideration for loading in liquid slurries for the same reason. Historically, micron-sized particles have been used for this application, but the recent large-scale manufacture of nano-sized particles by numerous vendors changes the extent of complete burning of Aluminum particles, the overall number of existing particles, and their average spacing dramatically. For this reason, collision process that may have been neglected in the past could be of significant importance in these flows.

The objective of the study in current period is to develop the complete models for the collision and breakup processes applicable to a simulation of the two phase flow in a rocket nozzle and carry a test simulation in a typical rocket converging-diverging nozzle to validate the modeling. For this purpose, laminar shearing/inertial collision models are developed considering compressible effects. The collision from these mechanisms was shown to be comparable to turbulent shearing/inertial collision.

MMD (Mass Mean Diameter) was predicted according to different droplet characteristics and pressure at nozzle inlet and the scales of nozzle. Shear and inertial-based models of collision and agglomeration were implemented into the model. Aerodynamic, hydrodynamic, and inertial breakup mechanisms were also implemented. These modeling are omitted in this report due to their complexity. A population balance equation to track local particle size distribution using Direct Quadrature Method of Moments was added to the model. A fast Eulerian approach for particle tracking was implemented.

To validate the models, the predicted results were compared to experimental data at the nozzle exit plane. The results were reasonably agreed with the empirical correlation. The simulation was very sensitive with the initial droplet condition (i.e. mean diameter and standard deviation of number distribution), therefore, the initial conditions of droplets should be chosen very carefully. Parameteric studies to assess the effects of particle concentration, chamber pressure and nozzle/motor size were also conducted and we report the effects of chamber pressure on particle interaction here.

### 3.2 Configuration

A series of simulation was performed to validate the code comparing the results to Crowe et al. (1963)'s experimental results and Hermsen (1981)'s correlation. Crowe et al.'s nozzle has a length of 5.2 cm and a inlet radius of 1.587 cm. The throat is located at 2.113 cm downstream from the inlet and its diameter is 1.27 cm. The corresponding area ratios of the throat to the inlet and the throat to the exit are 6.246. Figure 3.1 illustrates their nozzle geometries. Figure 3.2 highlights an axisymmetric unstructured mesh used in the computations for Shegal (1962)'s geometry. The nozzle has a length of 15.4 cm and a inlet radius of 6.35 cm. The throat is located at 12.6 cm downstream from the inlet. The corresponding area ratio of the throat to the inlet is 30.57 and the ratio of the throat to the exit is 2.43. The inlet geometry is horizontally smoothed out to remove additional disturbances caused by sharp geometry. A simulation is performed in a typical axisymmetric unstructured mesh form.

Accordingly, we constructed a test matrix for Crowe et al. (1963)'s experiments and a test matrix by varying the chamber pressure for Shegal (1962)'s cases. Tables 3.1 and 2 summarize the inlet conditions for gas and particle phases and nozzle scales. In case of nozzle configuration of Crowe et al. (1963), the chamber pressures are chosen to compensate pressure variation according to Hermsen (1981).
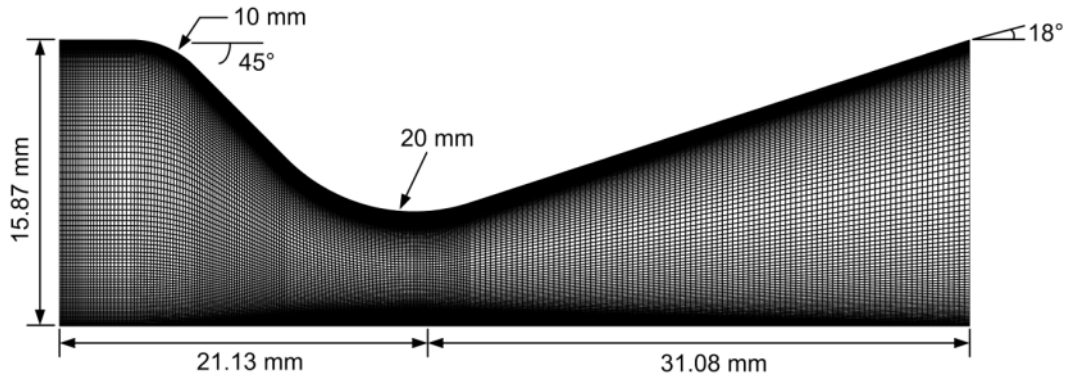


Figure 3.1 Schematic of the test nozzle geometry for Crowe et al. (1963)'s experiments (228x100 cell mesh)
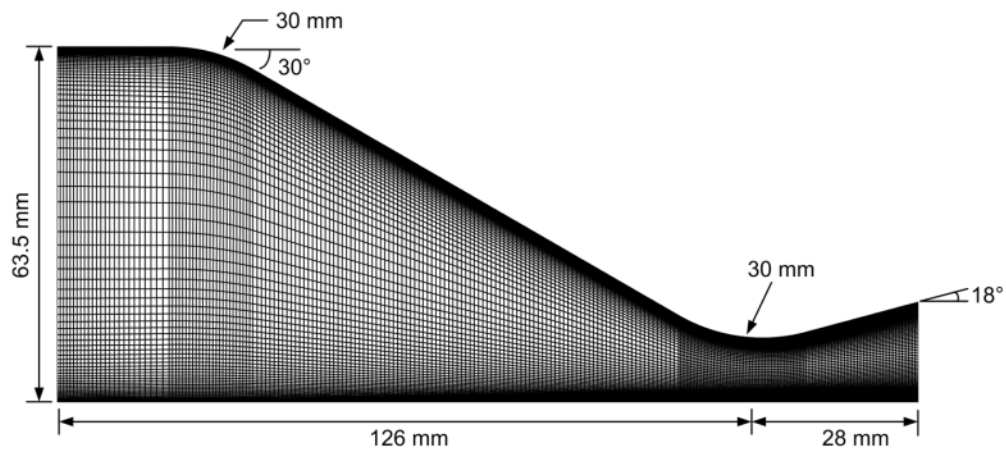


Figure 3.2 Schematic of the test nozzle geometry for Shegal (1962)'s experiment (245x80 cell mesh)

Table 3.1 The particle phase inlet boundary conditions – for Crowe et al. (1963)'s experiments

| Case no. | C-1-1 | C-1-2 | C-2 | C-3-1 | C-3-2 | C-3-3 | C-4-1 | C-4-2 | C-4-3 |
|---|---|---|---|---|---|---|---|---|---|
| $D_t$ (in.) | 0.5 | | | | | | | | |
| $\xi_c$ | 0.277 | | | | | | | | |
| $P_c$ (psi) | 110 | | 470 | 650 | | | 980 | | |
| $\tau_c$ (ms) | 15 | | | | | | | | |
| $n_{total}$ | 1.79e15 | 1.49e15 | 7.61e15 | 10.57e15 | 8.79e15 | 1.98e15 | 15.93e15 | 13.28e15 | 6.44e15 |
| $D_m$ ($\mu m$) | 0.361 | 0.385 | 0.361 | 0.361 | 0.385 | 0.634 | 0.361 | 0.385 | 0.490 |
| $\sigma_s$ ($\mu m$) | 0.456 | | | | | | | | |

Table 3.2 The particle phase inlet boundary conditions – chamber pressure variation for Shegal (1962)'s case

| Case no. | P-1 | P-2 | P-3 | P-4 | P-5 | P-6 | P-7 | P-8 |
|---|---|---|---|---|---|---|---|---|
| $D_t$ (in.) | 0.904 | | | | | | | |
| $\xi_c$ | 0.240 | | | | | | | |
| $P_c$ (psi) | 150 | 250 | 350 | 450 | 550 | 650 | 750 | 850 |
| $\tau_c$ (ms) | 4.15 | | | | | | | |
| $n_{total}$ | 5.08e15 | 8.43e15 | 11.83e15 | 15.22e15 | 18.6e15 | 22.0e15 | 25.37e15 | 28.75e15 |
| $\lambda$ (1/m) | 4804660.751 | | | | | | | |

### 3.3 Model Validation

A series of simulations was carried out to predict mass mean diameter at nozzle exit in the nozzle configuration given by Crowe et al. (1963). The small solid rocket motors are fired into the collection tank with the nozzle [Crowe et al. (1963)] and without nozzle [Crowe et al. (1966)] to assess the particle conditions obtained directly from the chamber. Crowe et al (1963)'s experiments and Hermsen (1981)'s correlation for current simulations and Crowe et al's experiments are plotted in Figure 3.3. The chamber pressure was changed by varying the propellant burning area with a fixed nozzle attached. The experimental chamber pressures are approximately 130, 320, 570, 900, and 1000 psi. According to Crowe et al. [50], they observed the chamber pressure variation during tests, therefore, we chose the pressure values given by Hermsen (1981) to account for the pressure variation. The chamber pressures of simulations are 110, 470, 650, and 980 psi and the corresponding case numbers are C-1-1 to 2, C-2, C-3-1 to 3, and, C-4-1 to 3, respectively. The horizontal lines associated with Crowe et al. (1966)'s experimental results on nozzle inlet indicate the pressure variation during experiments. The vertical bars represent 35% error bounds of Hermsen's correlation for each computational case.

The spatially weighted average of mass mean diameter at nozzle exit plane is obtained from the simulation. At 110 psi, the separation occurs in the divergent section, accordingly no particle zone creates. The averaging is taken over particles in the main flow stream at this pressure. The predicted results are presented in figure 4.4.1 and we observed a good agreement between the measured and predicted particle size over 500 psi chamber pressures. In case of 650 psi chamber pressure, the minimum predicted mass mean diameter at 650psi is 11% less than the minimum experimental value at 570 psi chamber pressure and the maximum predicted mass mean diameter is 20% less than the maximum experimental value. Comparing the predicted mass mean diameter at 980 psi and experimental value at 900 and 1000 psi, the differences are less than 9%. Considering the error bounds of correlation, a good agreement is observed between the correlation and predicted particle size over 500 psi chamber pressures.
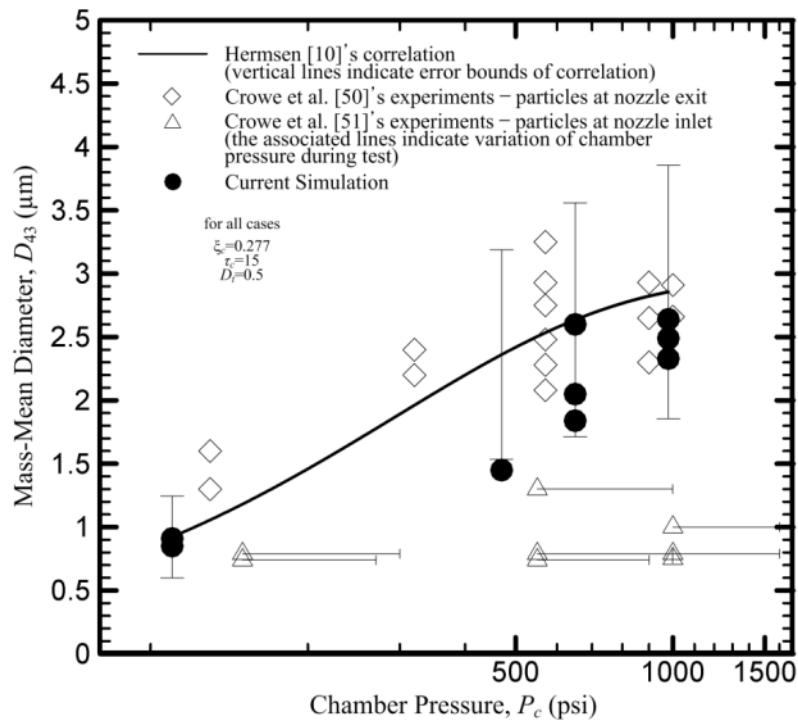


Figure 3.3 Predicted and measured mass mean diameter at nozzle exit planes
of particles in nozzle configuration by Crowe et al. (1963)

3.4 <u>Chamber Pressure Effects</u>

The current modeling described previously was compared here to Hermsen's correlation and the dependence of mass mean diameter on the chamber pressure level was analyzed. A series of simulations was performed to compare the results to the correlation under the nozzle configuration used by Shegal (1962) for 150psi chamber pressure. The corresponding case numbers are from P-1 to 8

and the chamber pressures are varied from 150psi to 850psi. The nozzle inlet conditions reported by Fein [54] for Shegal's 150 psi case are 0.240 of the particle concentration, 4.15 of the particle residence time, and 0.79 µm of the mass mean diameter. Using these initial conditions, the simulation performed for various pressures and Hermsen's correlation is calculated.

Figure 3.4 shows the effect of the chamber pressure on the mass mean diameter along the axis and wall, and at throat and nozzle exit plane. The (a) in Figure 3.4 shows that the largest growth rate occurs in the convergent section, specially, the most growth occurs in short region in front of the nozzle throat. The mass mean diameter after passing the throat shows little growth in divergent section at low chamber pressure but the mass mean diameter after the throat shows significant growth in divergent section at high chamber pressure. The breakup mechanism due to slip between a particle and gas might be balanced with collision in far downstream from the throat, then the mass mean diameter approaches a certain value in this region.

Figure 3.4b shows the variation of mass mean diameter in the boundary layer and it shows more complicated variation than centerline case. It is observed that there exist three peaks for lower pressure cases. The first peak corresponds to the recirculation region which leads to significant shearing motion of flow then shearing collision of particles. The second peak corresponds to the maximum mass mean diameter in the entire domain of lower pressure cases and this peak diminishes as the chamber pressure increases. Accordingly, the second peak is not observed in 850 psi case. The second peak comes from the wall impingement region in convergent section of nozzle. The third peak is the location where the breakup process becomes dominant. After passing the throat, the particles still experience growth and then breakup process becomes larger than collision at a certain point and results in the third peak.  The growth rate after the throat increases as the chamber pressure increases. When the chamber pressures are lower than 450 psi, the third peak is lower than the second peak. The reduction rate after the third peak is large with high pressure at this region. The interesting observation is that this peak is located far downstream from the throat with low chamber pressure and located almost at the throat with high chamber pressure. Unlike to the simulations on Crowe et al.'s nozzle configuration, no particle detachment is observed as explained in previous section.

Figure 3.5 shows the variation of the mass mean diameter in radial direction at throat and nozzle exit plane. It is clearly observed that the large amount of growth occurs within boundary layer due to flow shearing and it occurs more in higher pressure cases than lower pressure case.

The averaged mass mean diameter at nozzle exit is compared with Shegal (1962)'s experiments, Crowe and Willoughby (1967)'s prediction, and Hermsen (1981)'s correlation in Figure 3.6. The predicted results are mostly less than the measured results by Shegal. However, Dobbins and Strand (1969) lately indicated that Shegal's experimental results did not agree with other measurements. Dobbins and strand found that the particle size increases by a factor of 1.7 with a ten-fold increase while Shegal's experimental results gave increases by a factor of 5 with a ten-fold increase, approximately. Therefore, it may not be meaningful to compare the prediction with Shegal's results. Crowe and Willoughby's

calculation considering the slip velocity between a particle and surrounding gas and the momentum exchange in collision also had the less values than Shegal's results.

Over all chamber pressures, the variation trend is very similar to Hermsen's correlation, but the predicted results are larger than the results from Hermsen's correlation. However, the predicted values are within the error bounds of Hermsen's correlation (35%) over 500 psi chamber pressure and slightly over 35% under 500 psi. In addition, as explained above, Shegal reported the larger mass mean diameter than other studies. Because he used the same technique to obtain the particle size directly from the motor, his results might have a larger particle size than the actual size. Therefore, we expect that the resultant particle size using the actual inlet particle size may completely fall in the error bounds of Hermsen's correlation.
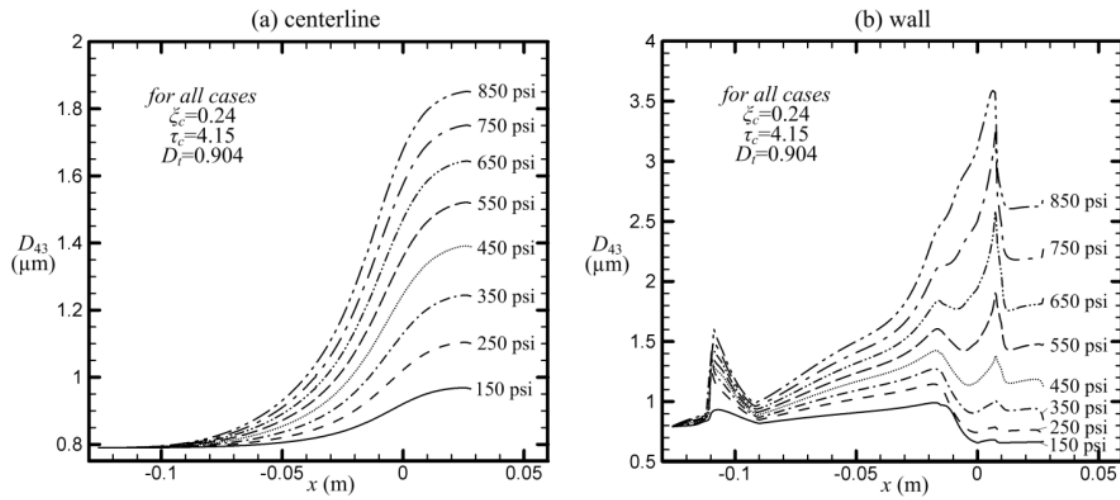


Figure 3.4 Axial variation of the predicted mass mean diameter along the centerline and wall according to chamber pressure variation
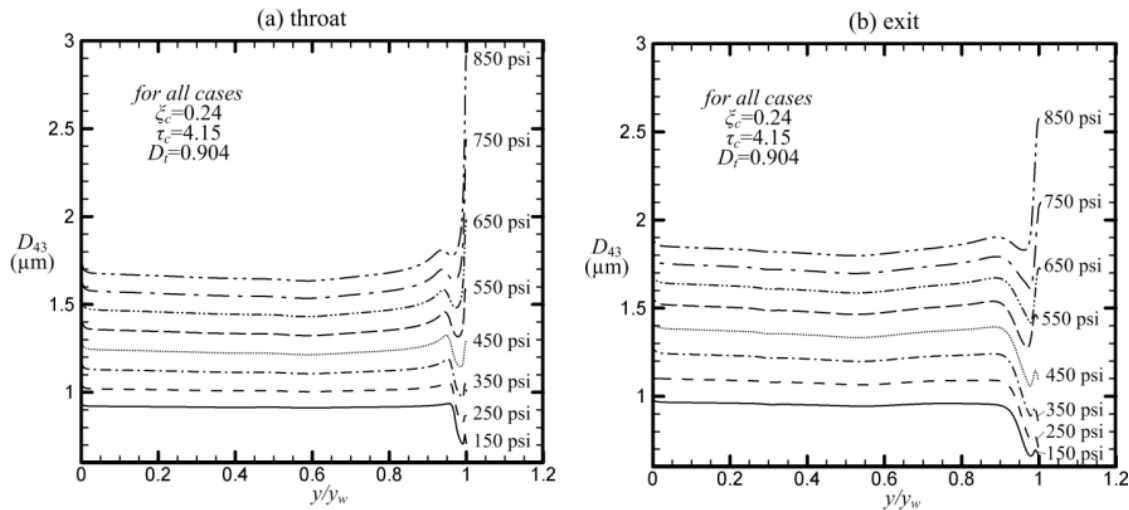


Figure 3.5 Radial variation of the predicted mass mean diameter at throat and nozzle exit plane according to chamber pressure variation
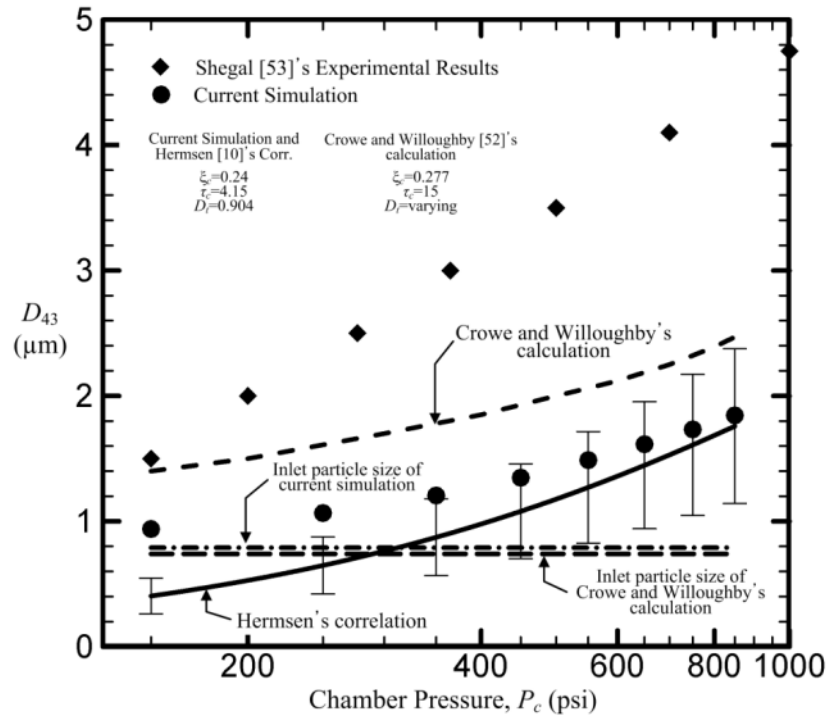
Figure 3.6 Predicted and measured mass mean diameter at nozzle exit planes in Shegal (1962)'s experimental condition – the effect of chamber pressure